# Chapter 5

# Brownian Dynamics

This chapter describes our first Brownian dynamics simulations, of a toroidal channel, using the analytical method described in the previous chapter and a Brownian dynamics algorithm due to van Gunsteren and Berendsen [72]. It provides a description of the theory and methods we use in performing BD simulations. The analytical method is around 5 times faster than the iterative method, but this is not yet fast enough to predict conductance. However, it is fast enough to allow the tracks of individual ions to be studied, and doing so yields a surprising amount of qualitative information about the operation of the model channel. Thus the chapter also serves as an intuitive introduction to the behaviour of our model channels, which is examined in more detail in the following chapters.

## 5.1 Model

### 5.1.1 Shape of the Channel

The channel boundary is a toroid with a minor radius of 40 Å and a major radius of 44 Å. The narrowest segment of this toroidal channel has the radius of 4 Å, and two vestibules extend 40 Å from the midline. The radius we selected for the constricted segment corresponds that of the potassium ion with its first hydration shell. The shape of the ACh channel determined by Toyoshima and Unwin [70] is better approximated by an hourglass than a toroid, but analytical solutions for Poisson's equation for such a dielectric boundary are not available.

Our model is only of the channel, and does not explicitly include the surrounding lipid membrane. The analytical solution is strictly for a toroidal dielectric boundary, and cannot be extended to include an infinite slab as well, as would be needed to represent the membrane. The model does have, however, a large outside radius (84 Å) compared to that of the ACh channel ($\sim$ 25 Å), and the exterior surface of the channel could be considered to include part of the surrounding membrane. We have ascertained that the

omission of the membrane makes virtually no difference to the potential in the pore. It is the inside boundary of the channel, between the water in the pore and the protein wall, that contributes the majority of the potential. To demonstrate the limited effect of the outside boundary, we reduced the outside radius of a catenary channel (similar to the one in Fig. 3.1) from 43 Å to 28 Å, while keeping all other dimensions constant. The potential barrier height was reduced only by 2 %. Similarly, when we increased the catenary channel's outside radius from 43 Å to 73 Å, the barrier height increased by less than 1 %.

### 5.1.2 Water as a Continuum

We treat the water as a continuum and the ions as individual entities. Individual ions are assumed to move under the influence of electrostatic forces emanating from other ions, fixed charges, the applied electric field and the dielectric boundary. In the Brownian dynamics simulations, the effects of solvation and the structure of water are taken into account by frictional and random forces. In applying the theory of macroscopic electrostatics to describe long range interactions between particles, we use the bulk dielectric constant. See section 3.1.4 for a discussion of the implications of using macroscopic electrostatic theory and the bulk dielectric constant.

### 5.1.3 Smooth Water-Protein Interface

We model the water-protein interface as a single, sharp and rigid boundary between dielectrics. In reality, however, the channel wall is not made of a structureless dielectric material. Instead, its surface is likely to be lined with hydrophilic and polar side-chains, although their type, orientation and density remain to be determined. Owing to the presence of these polar groups on the protein wall, there will be a gradual change in the orientation of the water molecules, those water molecules located nearer to the water-protein interface tending to be more ordered than those further away from it. The polar groups and the ordered water near the interface are not explicitly included in our model, being represented by the dielectric boundary. It is possible to treat the interface more accurately by assuming that there is a thin boundary layer with a dielectric constant intermediate between those of protein and water. We have shown elsewhere that the magnitude of error introduced by ignoring the intermediate dielectric layer is negligible [33]. Moreover, we show in the section 5.4.4 that ions in the vestibules tend to be near the central axis, away from the channel wall.

As with the treatment of water as a continuum, these simplified walls subsume the detailed molecular structure of the real protein. This is necessary to make the simulation work, but it risks error if the conductance of the channel depends on the detail of short range interactions between ions

and the protein walls.

### 5.1.4 Dipole Rings

We investigate how the permeation of ions across the channel is influenced by the presence and absence of dipoles on the protein wall. We assume that these charged moieties are located near the constricted region of the channel, as suggested by structural studies (*e.g.*, Ref. [71]), and represent them as a ring of 4 dipoles at each side of the membrane segment, oriented perpendicular to the central channel axis. These fixed charges represent the charged side chains thought to form a ring around the entrance of the constricted region, and their nearby counter charges. For convenience we adjust the amount of charge rather than the number or positions of the charges, but in reality their side chains would have one electron charge each. Polar groups located in the constricted segment of the channel that may rotate in and out to form temporary hydrogen bonds with an ion navigating across it, as found in gramicidin A pores, are not explicitly modeled in our toroidal channel.

### 5.1.5 Applied Electric Field

There are two ways of providing the driving force that can move the ion across the channel: a potential difference or a concentration gradient between the two faces of the channel. On a macroscopic level these two are equivalent, being coupled by the Nernst-Planck equation, and concentration differences are often expressed as an equivalent potential. On a microscopic level, however, the physical processes are very different. An electric potential gradient applies a force to every ion, causing it to acquire an average drift velocity. A concentration gradient causes no forces on the ions and no average drift velocity, but their random Brownian motion carries the ions down the concentration gradient. To mimic the real situation, the potential gradient should be generated by a diffuse cloud of unpaired positive ions, representing a surface charge density, in one reservoir and a cloud of unpaired negative ions in the other. The number of unpaired ions must be, to be consistent with the situation in real biological membranes, a small fraction of the total number of the ionic species present. Thus, the clouds of surface charges cannot be represented explicitly within the simulation unless the size of the simulation is expanded by a factor of 100. It is impractical to generate a potential difference with clouds of the ionic atmosphere, although this method is self-consistent and theoretically correct.

We therefore provide the driving force by applying an external electric field, which represents the average effect of the ionic clouds. From a number of current-voltage relationships obtained with a different number of ions in two reservoirs, we have ascertained that the reversal potential occurs

at a potential close to that predicted by the Nernst equation (the electrical potential needed to balance a particular combination of ionic concentrations, so that no current flows, is called the reversal potential: it can be predicted by the Nernst equation). In our simulation system, as in a macroscopic system composed of an ensemble of real biological channels, the force driving ions across the membrane can be provided either by an externally applied electric field or by a concentration gradient.

## 5.2 Theory

### 5.2.1 Langevin Equation

Brownian dynamics offers one of the simplest methods for following the trajectories of interacting ions in a fluid. The algorithm for BD is conceptually simple: the motion of the $i$ th ion with mass $m_i$ and charge $q_i$ is governed by the Langevin equation

$$m_i \frac{d\mathbf{v}_i}{dt} = -m_i \gamma_i \mathbf{v}_i + \mathbf{F}_R(t) + q_i \mathbf{E}_i. \tag{5.1}$$

The first two terms on the right-hand side of Eq. 5.1 describe the effects of collisions with the surrounding water molecules. The first term corresponds to an average frictional force with the friction coefficient given by $m_i\gamma_i$: $1/\gamma_i$ is the relaxation time constant of the system. The second term, $\mathbf{F}_R(t)$, represents the random part of the collisions and rapidly fluctuates around a zero mean. The frictional and random forces in Eq. 5.1 are connected through the fluctuation-dissipation theorem [61], which relates the friction coefficient to the autocorrelation function of the random force

$$m_i \gamma_i = \frac{1}{2kT} \int_{-\infty}^{\infty} \langle F_R(0) F_R(t) \rangle dt, \tag{5.2}$$

where $k$ and $T$ are the Boltzmann constant and temperature in degrees Kelvin, respectively. Here and throughout angular brackets denote ensemble averages. Finally, $\mathbf{E}_i$ in Eq. 5.1 denotes the total electric field at the position of the ion arising from (i) other ions, (ii) fixed charges in the protein, (iii) membrane potential, and (iv) induced surface charges on the water-protein boundary. This term in Eq. 5.1 is computed by solving Poisson's equation. Note that in three dimensions, Eq. 5.1 has to be solved for each cartesian component $(x, y, z)$ of the velocity.

Here we give the basic steps in solution of the Langevin equation that are implemented in the BD algorithm of van Gunsteren and Berendsen [72]. Using the the integrating factor $e^{\gamma t}$, the Langevin equation, Eq. 5.1, can be integrated from an initial time $t_n$ to $t$ to obtain for the velocity

$$v(t)\, e^{\gamma t} - v(t_n)\, e^{\gamma t_n} = \frac{1}{m} \int_{t_n}^{t} [F(t') + F_R(t')]\, e^{\gamma t'} dt'. \tag{5.3}$$

Here and in the following, the indices referring to ions and Cartesian components are omitted for convenience. The integral over the random force in Eq. 5.3 can be obtained using the stochastic properties of $F_R(t)$. For the electric force, we Taylor expand $F(t)$ around $t_n$

$$F(t) = F(t_n) + \dot{F}(t_n)(t - t_n) + \ldots, \tag{5.4}$$

where $\dot{F}(t_n)$ denotes the derivative $F(t)$ at $t = t_n$. Here the first order expansion of $F(t)$ is sufficient as the positions in the BD algorithm are exact to third order. Substituting Eq. 5.4 in 5.3 and integrating the force terms gives

$$\begin{aligned} v(t) = v(t_n)\, e^{-\gamma(t-t_n)} &+ \frac{F(t_n)}{m\gamma}\left(1 - e^{-\gamma(t-t_n)}\right) \\ &+ \frac{\dot{F}(t_n)}{m\gamma^2}\left(\gamma(t-t_n) - 1 + e^{-\gamma(t-t_n)}\right) \\ &+ \frac{e^{-\gamma t}}{m}\int_{t_n}^{t} F_R(t')\, e^{\gamma t'} dt'. \end{aligned} \tag{5.5}$$

To find the position after a time step $\Delta t$, we need to integrate Eq. 5.5 once more from $t_n$ to $t_n + \Delta t$. Integration of all the terms in Eq 5.5 are straightforward except the last one which can be done by parts using $du = e^{-\gamma t}$ and $v$ as the integral of $F_R$

$$\begin{aligned} &\int_{t_n}^{t_n+\Delta t} \frac{e^{-\gamma t}}{m}\int_{t_n}^{t} F_R(t')\, e^{\gamma t'} dt' \\ &\quad = \frac{1}{m\gamma}\int_{t_n}^{t_n+\Delta t}\left[1 - e^{\gamma(t-t_n-\Delta t)}\right] F_R(t) dt \\ &\quad \equiv X_n(\Delta t), \end{aligned} \tag{5.6}$$

where we have defined the random variable $X_n(\Delta t)$, which has the same stochastic properties as $F_R(t)$. We refer to Ref. [72] for details of how $X_n(\Delta t)$ is implemented in the BD algorithm. Using Eq. 5.6, the position at time $t_{n+1} = t_n + \Delta t$ is found to be

$$\begin{aligned} x(t_{n+1}) = x(t_n) &+ \frac{v(t_n)}{\gamma}(1 - e^{-\tau}) + \frac{F(t_n)}{m\gamma^2}(\tau - 1 + e^{-\tau}) \\ &+ \frac{\dot{F}(t_n)}{m\gamma^3}\left(\frac{\tau^2}{2} - \tau + 1 - e^{-\tau}\right) + X_n(\Delta t). \end{aligned} \tag{5.7}$$

Here $\tau = \gamma\Delta t$ is a dimensionless parameter which signifies a diffusive regime when $\tau >> 1$ or a microscopic one when $\tau << 1$. A more convenient form for $x(t_{n+1})$, which does not involve the velocity, can be obtained by adding $e^{-\tau}$ times $x(t_{n-1}) \equiv x(t_n - \Delta t)$ to Eq. 5.7

$$x(t_{n+1}) = x(t_n)(1 + e^{-\tau}) - x(t_{n-1})e^{-\tau} + \frac{F(t_n)}{m\gamma^2}\tau(1 - e^{-\tau})$$

$$+ \frac{\dot{F}(t_n)}{m\gamma^3}\left(\frac{\tau^2}{2}(1+e^{-\tau}) - \tau(1-e^{-\tau})\right) + X_n(\Delta t) - X_n(-\Delta t)e^{-\tau}. \quad (5.8)$$

Similarly, a simple expression for the velocity follows by subtracting $x(t_{n-1})$ from Eq. 5.7

$$v(t_n) = \frac{2\gamma}{\sinh\tau}\left[x(t_{n+1}) - x(t_{n-1}) + 2\left(\frac{F(t_n)}{m\gamma^2} - \frac{\dot{F}(t_n)}{m\gamma^3}\right) \times (\sinh\tau - \tau) - X_n(\Delta t) + X_n(-\Delta t)\right]. \quad (5.9)$$

Eqs. 5.8 and 5.9 provide the basic input for the BD algorithm used in the simulations.

## 5.3 Methods

### 5.3.1 Algorithm

We solve the Langevin equation using the BD algorithm devised by van Gunsteren and Berendsen [72], which consists of the following computational steps:

- step 1. Compute the electric force $\mathbf{F}(t) = q_i\mathbf{E}_i$ acting on each ion at time $t_n$ and calculate its derivative $[\mathbf{F}(t_n) - \mathbf{F}(t_{n-1})]/\Delta t$.
- step 2. Compute a net stochastic force impinging on each ion over a time period of $\Delta t$ from a sampled value of $\mathbf{F}_R(t)$.
- step 3. Determine the position of each ion at time $t_n + \Delta t$ and its velocity at time $t_n$ by substituting $\mathbf{F}(t_n)$, its derivative $\mathbf{F}'(t_n)$ and $\mathbf{F}_R(t)$ into the solutions of the Langevin equation (Eqs. 5.8 and 5.9).
- step 4. Repeat the above steps for the desired simulation period.

An advantage of the above algorithm over some earlier ones is that one is not limited by the condition $\Delta t \ll 1/\gamma$. For the Na ions, this condition would require $\Delta t \ll 10$ fs, which would severely limit the applicability of BD to ion channels. With this algorithm only two factors limit the choice of $\Delta t$. The average distance a particle traverses in each time step must be small compared to the dimensions of the system. Also, the time derivative of the electric forces must be small relative to the absolute magnitude of the force. In a preliminary series of simulations, we have systematically increased the time step, $\Delta t$, from 25 fs to 1.6 ps and examined the motion of the test particle. As $\Delta t$ increased beyond 100 fs, the trajectory of the

test particle began to deviate systematically from that obtained with a short time step. In the current simulations, we have used $\Delta t = 50$ fs. Using the average thermal velocity for the sodium ions (see Fig. 5.2 A), the average displacement of ions in time $\Delta t$ is found to be about 0.25 Å. (The radius of the narrow segment of the toroidal channel, in contrast, is 4 Å.) The change in the electric field during this time step is calculated to be at most a few percent.

### 5.3.2 Reflective Boundaries

When the ionic concentration in the reservoirs is high, ions at times are able to jump large distances and end up very close to another ion. The forces at the next time step in such instances can be very large and the affected ions may leave the system. To correct this problem, we check ion-ion distances at each time step. If two ions are within a 'safe distance', chosen to be 3/4 of the sum of the ionic radii, then their trajectories are traced backwards in time until such a distance is exceeded. By performing these checks and corrections, the system is well behaved over the simulation, even for very high concentrations. Such a minor re-adjustment of the position of an ion is needed about once every 100 time steps when the reservoirs and the channel contain 52 ions. The steep repulsive force at the dielectric boundary due to the image charges and the ion-protein potential is usually sufficient to prevent ions from entering the channel protein. We ensure that no ions appear inside the channel protein by erecting an impermeable hard wall at 1 Å from the water-protein interface. Any ion colliding with this wall is elastically scattered. A similar hard wall is implemented for the reservoir boundaries.

### 5.3.3 Physical Parameters

The following physical parameters were employed in our calculations for the toroidal channel:
Dielectric constants: $\epsilon_{\text{water}} = 78.54, \quad \epsilon_{\text{prot}} = 2.$
Masses: $m_{\text{Na}} = 3.8 \times 10^{-26}$ kg, $\quad m_{\text{Cl}} = 5.9 \times 10^{-26}$ kg.
Diffusion coefficients: $\text{D}_{\text{Na}} = 1.33 \times 10^{-9}$ m$^2$ s$^{-1}$, $\text{D}_{\text{Cl}} = 2.03 \times 10^{-9}$ m$^2$ s$^{-1}$.
Relaxation time constants, $\gamma^{-1}$: $\gamma_{\text{Na}} = 8.1 \times 10^{13}$ s$^{-1}$, $\quad \gamma_{\text{Cl}} = 3.4 \times 10^{13}$ s$^{-1}$.
Ion radii, $r_{\text{Na}} = 0.95$ Å, $\quad r_{\text{Cl}} = 1.81$ Å.
Room temperature: $T_r = 298$ °K.
Boltzmann constant: $k = 1.38 \times 10^{-23}$ JK$^{-1}$.

Frictional coefficients $\gamma$ are derived from the diffusion coefficients $D$ by the Nernst-Einstein relationship $D = kT/m\gamma$, that is $\gamma = kT/mD$. However, since the diffusion coefficients were calculated from the limiting equivalent conductivities $\lambda_0$ (from Robinson and Stokes [63]) by another form of

this relation, $D = RT\lambda_0/zF^2$, the frictional coefficients are in effect calculated from $\gamma = zeF/m\lambda_0$. The limiting equivalent conductivities are strictly only valid in the limit of infinite dilution. At the concentrations of 150-300 mM used in the simulations the difference is around 10% (see appendix 11.2 of reference [63]). This difference is due to the effect of high concentrations of ions on the structure of bulk water. Since the confined spaces of a channel may have a completely different (and unfortunately unknown) effect on water structure and diffusion coefficients, we do not include compensation for the higher concentrations.

### 5.3.4 Testing

To confirm that the behavior of the interacting ions deduced from simulations accords with the physical reality, we examined the mean-square displacement, $\langle x^2 \rangle$, the velocity distribution, and the velocity autocorrelation function, $\langle v(0)v(s) \rangle$. These simulations were carried out on the toroidal channel with two reservoirs, as described in section 5.1, except that the dielectric constant of the protein was set equal to that of water. Thus ions are scattered elastically from the boundary but otherwise there were no forces acting on them due to the change in the dielectric constants.

Theoretically, the mean square displacement $\langle x^2 \rangle$ should obey the relation

$$\langle x^2 \rangle = \frac{2kT}{m_i \gamma_i} t, \quad \text{for} \quad t \gg \gamma_i^{-1}. \tag{5.10}$$

In Fig. 5.1, the mean-square displacement obtained for sodium (filled circles) and chloride (open circles) from one simulation lasting 500,000 time steps (25 ns of real time) is plotted against time. These are compared with the predicted slopes obtained from Eq. 5.10 (solid lines in Fig. 5.1). The simulation results are about 7% lower than the predicted values for a bulk solution, which is probably due to ions scattering back from the boundary, retarding their free diffusion.

Figure 5.2 A shows the velocity distributions of sodium and chloride ions in the system. From the equipartition theorem, the equilibrium distribution of the velocity should be Maxwellian of the form [61]

$$F(v)dv = 4\pi n \left[ \frac{m_i}{2\pi kT} \right]^{1/2} \exp(-m_i v^2/2kT)\, v^2 dv, \tag{5.11}$$

where $n$ is the number density of ions and $F(v)dv$ is the mean number of ions per unit volume with a speed in the range between $v$ and $v + dv$. The velocity distributions obtained from the BD simulations are seen to match closely those computed from Eq. 5.11 (solid lines).

The velocity autocorrelation function is of the form [61]

$$\langle v(0)v(s) \rangle = \frac{kT}{m_i} \exp(-\gamma_i |s|). \tag{5.12}$$

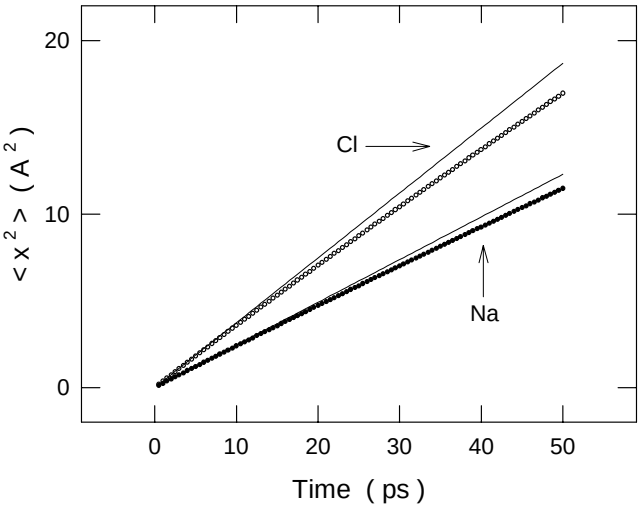


Figure 5.1: Test of the Brownian dynamics algorithm: mean-square displacements. The mean-square displacements, $\langle x^2 \rangle$, of chloride ions ($\circ$) and sodium ions ($\bullet$) are plotted against time. The solid lines superimposed on the graph are derived from the relation, $\langle x^2 \rangle = 2$ D $t$ where the diffusion coefficients D for sodium and chloride ions are given in section 5.3.3. The mean-square displacements determined from simulated data deviated systematically from the predicted values. The reason for these discrepancies between the theoretical and measured values is given in the text.

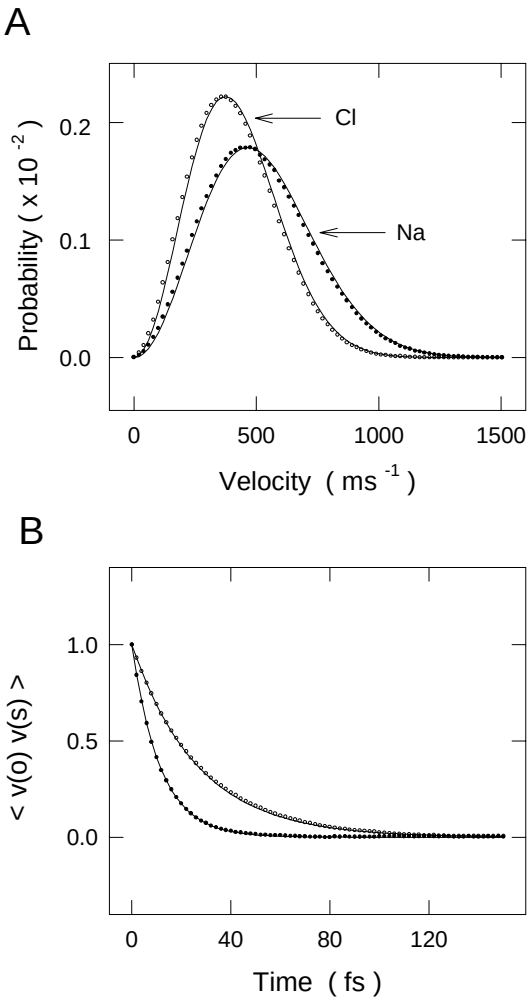


Figure 5.2: Test of the Brownian dynamics algorithm: velocity functions. (A). The Maxwellian velocities distributions, $F(v)dv$, of sodium (•) and chloride (○) ions are normalized for the volume of phase space and plotted. The solid lines superimposed on the measured distributions are calculated from Eq. 5.11. (B). The velocity autocorrelation functions, $\langle v(0)v(s)\rangle$, for sodium (•) and chloride (○) ions decayed exponentially. The continuous lines are calculated from Eq. 5.12.

Thus, regardless of the initial velocity, the successive velocities will be correlated over a time interval of the order of $1/\gamma_i$, the relaxation time constant of the system. To verify Eq. 5.12, we determined the velocities of the ions at every 0.5 fs for 50,000 time steps. The autocorrelation functions shown in Fig. 5.2 B decayed exponentially, as predicted from Eq 5.12 (solid lines). Again, filled and open circles represent the calculated values of sodium and chloride ions, respectively.

From a number of these preliminary simulations, we conclude that the BD algorithm faithfully characterizes the motion of interacting ions in a fluid confined with a reflective boundary.

## 5.4 Results

### 5.4.1 Repulsive Dielectric Force

When deliberately placed inside the toroidal channel, ions were rapidly expelled to the reservoir within 1 to 2 ns. A sodium ion in the system, the test particle, was placed inside the channel, on the central axis of the pore at $z = 5$ Å, as indicated in the inset of Fig. 5.3. The initial locations of the remaining 99 ions were randomly assigned. The position of the ion placed in the channel, as well as the remaining ones in the system, was calculated at each discrete time step of 50 fs for 50,000 time steps. Thus, the total simulation time for one such trial was 2.5 ns. These computational steps were repeated 5 times. For each trial, the positions of all ions, except the test particle, at the last time step in the preceding trial were used as the initial starting positions of the subsequent trial. The same series of simulations were repeated for a chloride ion. A representative simulation from each set is shown in Fig. 5.3 A, where the trajectories of the sodium and chloride ions placed in the channel are plotted against time. Each of the consecutive 200 points plotted in Fig. 5.3 A represents an average of 100 time steps or 5 ps. The ensemble averages of 5 trials each for the sodium and chloride ions are illustrated in Fig. 5.3 B. Here the positions of the ions during the entire simulation period of 2.5 ns are plotted.

The speed with which the ionic species were ejected was different. Owing to their higher mobility, chloride ions were consistently expelled faster than sodium ions. Once they were ejected from the channel, these or any other ions in the upper reservoir rarely, if ever, drifted back inside of the channel. These simulations demonstrate that the repulsive dielectric force arising from induced surface charges on the protein wall renders the channel vestibule for the most part devoid of ions.

The magnitude of the repulsive force presented to an ion by the dielectric boundary is sufficiently large that a driving force provided by a transmembrane potential of 100 mV cannot counteract it. This conclusion is based on the following series of simulations. After placing a sodium ion at $z = -20$ Å

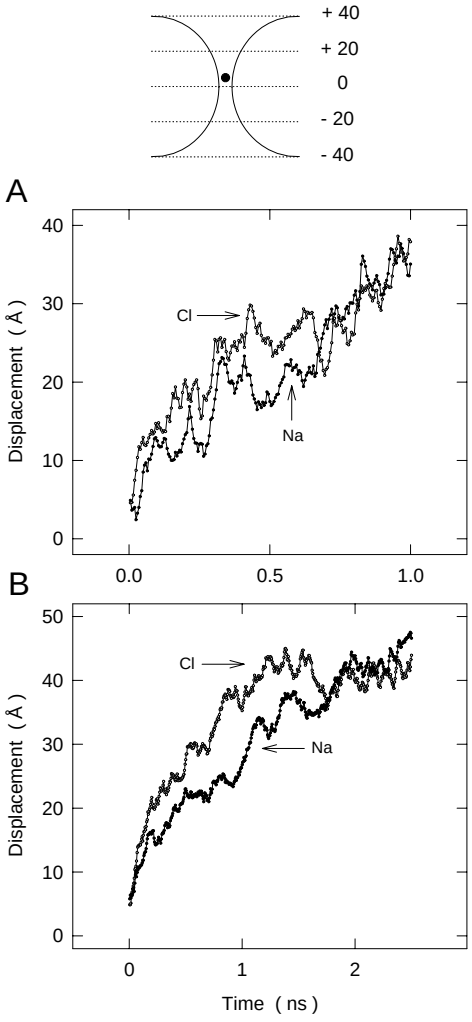


Figure 5.3: Ejection of ions from the vestibule. The filled circle in the inset indicates the initial position of the input ion at the beginning of each set of simulations. Each simulation lasted 50,000 time steps. For clarity, the reservoirs and the remaining 99 ions are not shown. (A). The graphs show the positions of a sodium ion (•) and a chloride (○) ion during the first 1 ns. Each point represents the average of 100 consecutive time steps or 5 ps. From the starting position at $z = 5$ Å, both anion and cation rapidly moved out from the narrow segment of the channel towards the upper reservoir. (B). The mean positions at each consecutive 5 ps are averaged over 5 trials and then plotted against time.

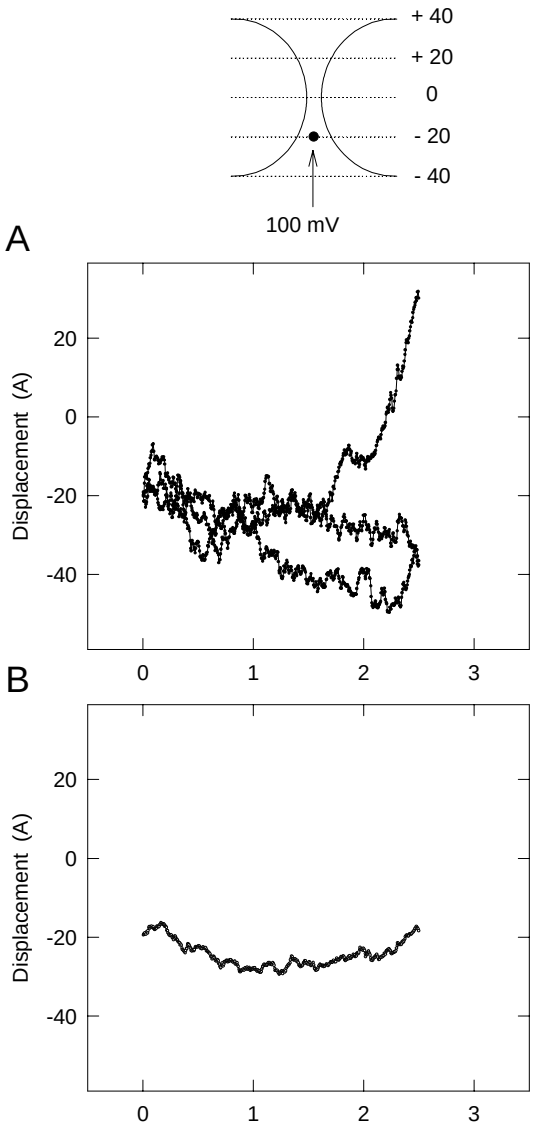


Figure 5.4: Repulsive dielectric force and applied electric field. After placing the test sodium ion at $z = -20$ Å, an electric field of $10^7$ V/m was applied in the positive $z$ direction. Shown in (A) and (B) are, respectively, three examples of the trajectories of the test particle and the average trajectory of 9 trials.

(see the inset of Fig. 5.4), an electric field of $10^7$ V/m was applied across the channel in the positive $z$ direction. In the absence of any dielectric force opposing it, the ion would have drifted across the channel within 2 ns. In Fig. 5.4 A, 3 trajectories of a sodium ion are illustrated. Again, each point represents the average of 100 consecutive time steps, or 5 ps. In 7 out of 9 trials, the ion placed at $z = -20$ Å was either ejected from the channel and entered the lower reservoir or remained in the channel vestibule. In the remaining 2 trials, the ion was able to penetrate into the other side of the channel. The average of all 9 trials is shown in Fig. 5.4 B. The driving force provided by the applied electric field was effectively opposed by the repulsive dielectric force.

### 5.4.2 Dipoles in the Transmembrane Segment

The previous simulations indicate that, unless the potential barrier arising from the induced surface charges is counteracted by fixed charges or dipoles in the channel protein, ions in the majority of trials are not able to permeate the channel. In the following series of simulations, we explored the effects of such residual charges on ion permeation, by placing a ring of four dipoles at each end of the transmembrane segment, as described in the section 5.1.4 (see the inset of Fig. 5.5). The total strength of the dipoles on each side was $100 \times 10^{-30}$ Cm. This configuration of dipoles would be attractive to cations but would create an additional repulsive force for anions.

Figure 5.5 demonstrates the effects of dipoles on the motion of sodium and chloride ions that were deliberately placed inside the channel. A chloride ion placed at $z = 5$ Å along the central axis was expelled from the channel vestibule. In contrast, a sodium ion, when placed at the same position, remained in the vicinity of the dipoles, where the charges of the opposite polarity were providing an attractive potential for the ion. Sample trajectories of a chloride ion (open circles), and a sodium ion (filled circles) are shown in Fig. 5.5 A. The trajectories shown in Fig. 5.5 B are the averages of 5 such trials. Averaging reduced the fluctuations, making the main trend clearer. Thus, a chloride ion was expelled from the channel rather quickly (in less than a nanosecond). For a sodium ion, on the other hand, the dipoles have eliminated the repulsive dielectric force that would have impinged on it, and hence it diffused freely in the channel.

### 5.4.3 Permeation of Ion Through the Channel

The channel that had been impermeable to both cations and anions (see Fig. 5.4) becomes a cation-selective channel once dipoles are placed in the transmembrane segment such that their negative poles would face the channel lumen. In Fig. 5.6 A, we illustrate the mean positions of a sodium ion during successive 5 ps steps as it moves across the channel under the in-

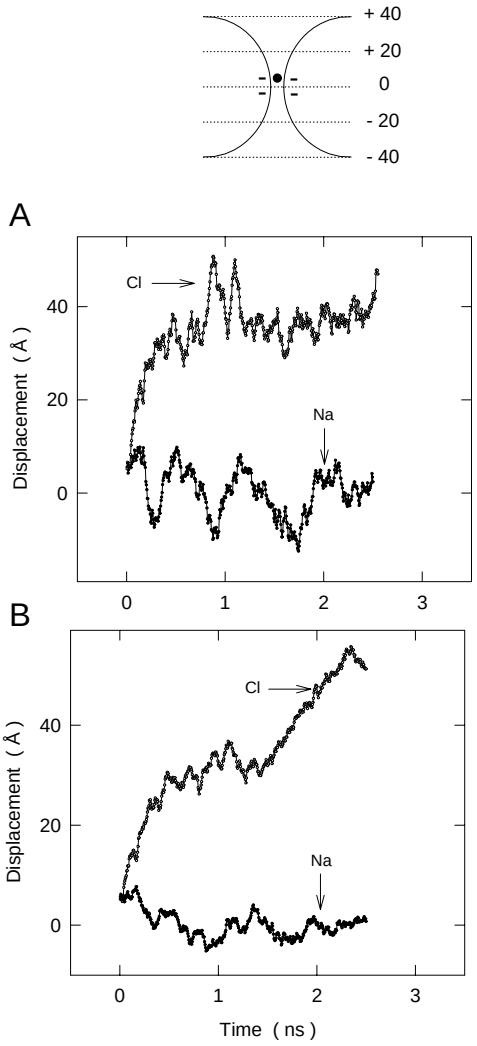


Figure 5.5: Cancellation of repulsive force by dipoles. The test particle, placed at $z = 5$ Å, was released and its positions during the subsequent 2.5 ns were plotted. The procedures of simulations were identical to those in Fig. 5.3, except that 4 dipoles with the total moment of $100 \times 10^{-30}$ Cm were placed on each side of the midline. The dipoles were placed in the channel protein such that their negative poles would face the lumen. (A). The trajectory of a chloride ion (○) obtained from one trial shows that it was rapidly ejected from the channel. In contrast, a sodium ion (●) remained in the constricted segment of the channel. (B). The trajectories for the test ions, open circles for chloride and filled circles for sodium, are obtained by averaging 5 successive trials.

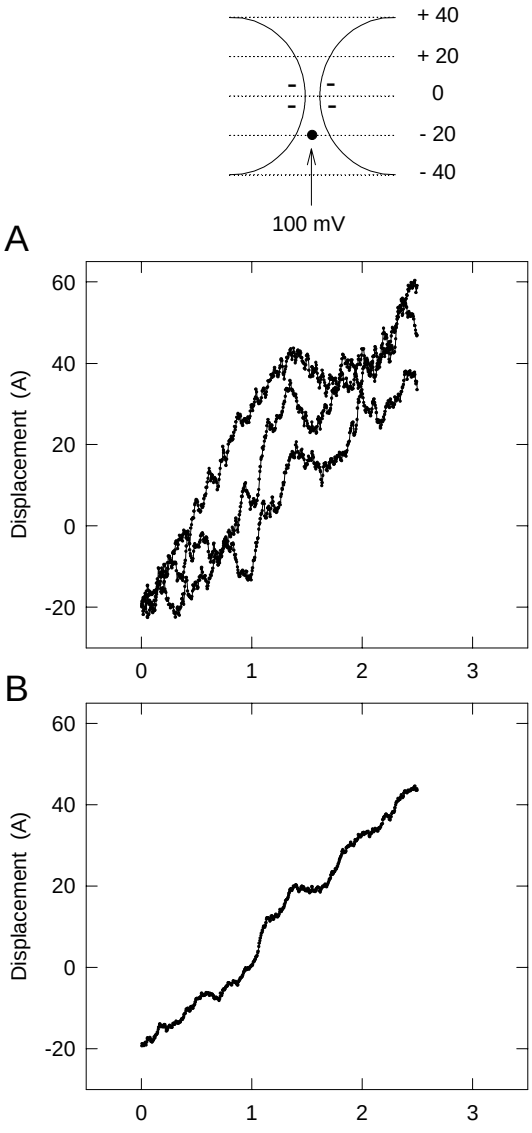


Figure 5.6: Permeation of sodium ions across the channel. A sodium ion was placed at $z = -20$ Å, as indicated in the Inset, and then a potential difference of 100 mV was applied across the channel. Dipoles on each side of the transmembrane segment had the total moment of $100 \times 10^{-30}$ Cm. (A). Three single trajectories show that the test ions successfully traversed the channel under the influence of the driving force. (B). The trajectory illustrated are the average of 9 trials. The mean drift velocity of the particles was 2.6 m $s^{-1}$.

fluence of an applied electric field of $10^7$ V/m. The three trajectories illustrated in the figure were obtained from the first three consecutive trials. The strength of the dipoles on each side of the transmembrane segment was $100 \times 10^{-30}$ Cm. In all 9 such attempts, a sodium ion, when released from $z = -20$ Å, successfully navigated across the channel. The trajectory averaged over 9 trials is shown in Fig. 5.6 B.

The sodium ion in these simulations had an average drift velocity of 2.6 m/s in the channel, which is about 5 times faster than that of a sodium ion in bulk electrolyte solutions moving under the influence of the same applied potential gradient. In part this is because the electric field in the constricted segment of the channel, far from being constant, is enhanced by the dielectric boundary and the presence of dipoles (see Ref. [42]). Also noteworthy in Fig. 5.6 is that the ion was not detained at the two regions where the rings of dipoles were located, indicating that the potential well created by them was not deep enough to trap the ion in it for a prolonged period of time.

### 5.4.4 Trajectory of Ions

The path taken by an ion as it journeys across the channel is predominantly along the central axis. Figure 5.7 shows snapshots of the positions of a sodium ion as it traversed across the channel under the influence of an electric field of $10^7$ V/m and in the presence of dipoles of strength $100 \times 10^{-30}$ Cm (these are the same simulations mentioned in Fig. 5.6). Each dot in the figure represents the location of the ion on the $z$- and $x$-axes averaged over 100 time steps. In the first example (Fig. 5.7 A), the ion was slightly deflected towards the dipoles as it moved across the transmembrane segment. In the second and third examples (Fig. 5.7 B, 5.7 C), the ions spent longer periods of time in the vicinity of the rings of dipoles, as indicated by the densities of dots. We have not expected, nor have we found, that an ion would bind to binding sites on the channel protein. These findings are in accord with those reported by Bek and Jakobsson [8].

## 5.5 Discussion

Despite their preliminary nature, the results in this chapter suggest a qualitative model for conductance in ligand gated cation channels. Although the analytical method is not fast enough to allow the prediction of conductance, by analyzing the trajectory of individual ions we have demonstrated some important points about our model channel. Without dipoles in the channel wall, the electrostatic barrier created by the channel is sufficient to repel ions from the vestibules and neck, preventing ions from crossing the channel even when a realistic driving force is applied (Figs. 5.3 and 5.4). However,

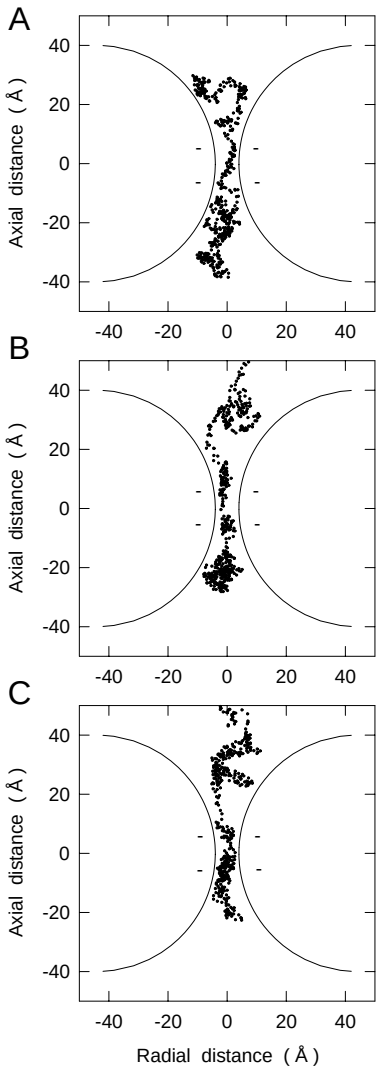


Figure 5.7: The path of ions. The mean positions of the test ions, as they navigate across the channel, are indicated as dots. Each dot represents the average of 100 consecutive positions of the cation, as it drifts across the pore. The data were derived from those illustrated in Fig. 5.6. Three different examples are shown. The small horizontal bars inside the torus boundary indicate the position of the negative ends of the dipoles.

if dipoles are added to the neck region with appropriate strengths and orientations, then the barrier is removed for cations, and they are able to cross the channel (Figs. 5.5 and 5.6). These same dipoles increase the barrier for anions, which are rejected from the channel even more quickly than was the case without dipoles (Fig. 5.5).

The picture that emerges for a ligand gated cation channel is of a device which provides a path for cations by removing the electrostatic barrier of the membrane. The wide vestibules and neck provide water which surround the ion, and reduce the barrier due to dehydration. Some of the barrier remains, however, especially in the neck region, where the pore is narrowest. Dipoles in the neck region overcome this remaining barrier, and cations are able to move through the channel by rapid diffusion. The result is a channel with a large conductance, that is highly selective for anions over cations, but not very selective between cations. This picture is consistent with structural studies, which suggest the wide vestibules (around 12 Å radius) and neck (around 4 Å radius), and the dipoles in the neck region [70, 71, 22]. It is also consistent with patch clamp studies, which demonstrate the large conductance and selectivity for cations (but not among cations) of this class of channel [34, 27, 2]. The Brownian dynamics simulations begin to show how the channel works, how the structural parameters are connected to the conductance characteristics.

Some doubts remain, however. Trajectories of individual ions give a good intuitive feel for the operation of the channel, but cannot yield quantitative predictions of conductance or its relation to structural parameters (such as dipole strength). Although the model is based on realistic physical assumptions, it contains many simplifications, and needs to be tested against experiment before it can be fully believed. For this to happen it needs to be capable of making quantitative predictions. Another area of concern is the effect of the other ions. These are included in the simulations, but the initial placement of the ion under examination is artificial, rather than emerging out of the simulation. The other ions may not have time to react to such a placement, and so shielding by counterions may have been ignored. This is an important point, since the Poisson-Boltzmann and Poisson-Nernst-Plank techniques predict that such shielding completely removes the electrostatic barrier, without any need for compensating dipoles. We have done equilibration tests which indicate that this is not the case [45], but a fully convincing demonstration requires a much longer simulation, in which the ions could enter and leave the channel in a natural and realistic manner. Thus both of these doubts could be removed by sufficiently long simulations, which would be possible if only the electrostatic system could be solved more rapidly. The next chapter describes how this can be achieved.

# Chapter 6

# Lookup Table Method

The BD algorithm requires calculation of electric forces acting on ions at each time step. Given the positions of ions, this can be achieved by solving Poisson's equation for an appropriate boundary. However, as emphasized above, this direct approach is computationally too expensive to be useful in the long time-scale simulations necessary for the calculation of conductance. Here we adapt an alternative method where the electric field and potential are pre-calculated on a grid of points for various configurations, and the results are stored in a number of lookup tables. During simulations, the field and potential at desired points are reconstructed by interpolating between the table entries. Compared to the analytical solution of Poisson's equation in toroidal coordinates, the lookup method is 60 times faster. The lookup method has the further advantage that one is not restricted to a toroidal channel: numerical solutions of Poisson's equation for more realistic channel shapes can be as easily stored in tables.

## 6.1 Components of the Potential

For calculational purposes, it is convenient to break the total electric potential $V_i$ experienced by an ion $i$ into four pieces

$$V_i = V_{S,i} + V_{X,i} + \sum_{j \neq i} V_{I,ij} + \sum_{j \neq i} V_{C,ij}, \tag{6.1}$$

where $V_{S,i}$ is the self potential due to the surface charges induced by the ion $i$ on the channel boundary and $V_{X,i}$ is the external potential due to the applied field, fixed charges in the protein wall, and charges induced by these. The next two terms in (6.1) take the influence of other ions into account, namely, $V_{I,ij}$ is the image potential due to the charges induced by the ion $j$, and $V_{C,ij}$ is the Coulomb potential due to the ion $j$, which is computed directly from

$$V_{C,ij} = \frac{1}{4\pi\epsilon_0} \frac{q_j}{\epsilon |\mathbf{r}_i - \mathbf{r}_j|}, \tag{6.2}$$

where $\mathbf{r}_i$ and $\mathbf{r}_j$ are the positions of the ions. The electric field experienced by the ion is decomposed in the same way

$$\mathbf{E}_i = \mathbf{E}_{S,i} + \mathbf{E}_{X,i} + \sum_{j \neq i} \mathbf{E}_{I,ij} + \sum_{j \neq i} \mathbf{E}_{C,ij}, \tag{6.3}$$

each field component being defined as in the potential (6.1).

## 6.2 Generalized Coordinates

The first three components in Eqs. (6.1) and (6.3) depend on the boundary and, in general, they are determined from numerical solutions of Poisson's equation (see chapter 3). Each of these components is calculated for a grid of positions and stored in separate tables. To allow rapid look up, the pre-calculated values must be on an evenly spaced grid. Because the use of a rectilinear grid would result in many wasted points and a jagged edge near the pore boundary, we use a system of generalized cylindrical coordinates in constructing the look up tables. In terms of the cylindrical coordinates $(r, \theta, z)$

$$r = \sqrt{x^2 + y^2}, \quad \theta = \tan^{-1}(y/x), \quad z = z, \tag{6.4}$$

the generalized coordinates $(\rho, \theta, \zeta)$ are defined as

$$\rho(r, z) = r/r_{\max}(z), \quad \theta = \theta, \quad \zeta(z) = (z - z_{\min})/(z_{\max} - z_{\min}), \tag{6.5}$$

where $r_{\max}(z)$ is the limiting radius of the pore, and $z_{\max}$ and $z_{\min}$ are the maximum and minimum $z$ coordinates for the system. The coordinates $\zeta$ and $\rho$ are normalized and cover the range $[0, 1]$. For $\theta$, we use the range $[-\pi, \pi]$ for convenience (see below). The limiting radius $r_{\max}(z)$ is offset from the pore wall by the radius of the smallest ion in the simulation, which defines the closest possible approach for an ion to the pore wall. Both the analytical and iterative methods are unable to calculate the potential *on* the pore wall, and both become less accurate the closer the boundary is approached, so it makes sense to set the limit of the generalized coordinates to the closest possible approach of an ion to the pore wall.

Besides providing a smooth edge near the boundary, the generalized coordinates also allow the cylindrical symmetry of the channel to be exploited. For example, the $\theta$ coordinate is redundant in the calculation of the self potential $V_{S,i}$, therefore it is stored in a 2 dimensional table $V_{2d}(\rho_m, \zeta_n)$. Similarly, the image potential $V_{I,ij}$ depends on the relative angle between the ions $i$ and $j$, and it is stored in a 5 dimensional table $V_{5d}(\rho_m, \zeta_n, \rho_{m'}, \zeta_{n'}, \theta_k)$. Due to reflection symmetry, $\theta_k$ and $-\theta_k$ lead to the same image potential. Hence $\theta_k$ in $V_{5d}$ covers only the range $[0, \pi]$. The fixed charges do not possess any particular symmetry, so the external potential $V_{X,i}$ is stored in a full 3 dimensional table $V_{3d}(\rho_m, \zeta_n, \theta_k)$. Here $\theta_k$ covers the whole range $[-\pi, \pi]$.

The electric field is stored in the same way as the potential, except that three values are required for each point in a table, one for each Cartesian component of the field. So while the field tables are indexed by the generalized coordinates, their contents are stored as Cartesian coordinates in the tables $\mathbf{E}_{2d}(\rho_m, \zeta_n)$, $\mathbf{E}_{3d}(\rho_m, \zeta_n, \theta_k)$, and $\mathbf{E}_{5d}(\rho_m, \zeta_n, \rho_{m'}, \zeta_{n'}, \theta_k)$. Note that, in principle, these results could be combined and stored in the same table. However, separate tables are more flexible and assist in minimizing the interpolation error, and are therefore preferred.

## 6.3 Lookup Algorithm

Once the positions of the ions have been converted to generalized coordinates, the extraction of the potential and field from the tables is relatively straightforward, and therefore fast. The values of the electric potential and field at the position of the ion are extracted from the tables by multidimensional linear interpolation, a simple algorithm that generalizes easily to dimensions greater than 2 [58]. Because the grid points are evenly spaced in the generalized coordinates, the appropriate indices can be found by division, rather than by a time consuming binary search. For an ion $i$ with charge $q_i$ at the position $\mathbf{r}_i = (\rho_i, \zeta_i, \theta_i)$ and another ion with charge $q_j$ at $\mathbf{r}_j = (\rho_j, \zeta_j, \theta_i)$, the potentials are given by

$$\begin{aligned} V_{S,i} &= \frac{q_i}{e} V_{2d}(\rho_i, \zeta_i), \\ V_{X,i} &= V_{3d}(\rho_i, \zeta_i, \theta_i), \\ V_{I,ij} &= \frac{q_j}{e} V_{5d}(\rho_i, \zeta_i, \rho_j, \zeta_j, |\theta_i - \theta_j|), \end{aligned} \tag{6.6}$$

where $V_{2d}(\rho_i, \zeta_i)$, $V_{3d}(\rho_i, \zeta_i, \theta_i)$, and $V_{5d}(\rho_i, \zeta_i, \rho_j, \zeta_j, |\theta_i - \theta_j|)$ are obtained by applying the interpolation algorithm to the 2 dimensional self potential table, the 3 dimensional external potential table, and the 5 dimensional image potential table, respectively. The self potential and image potential tables are constructed assuming a positive unit charge as source, so the results are rescaled to the actual source charge after lookup.

The symmetries used to reduce the size of the tables require that the recovered electric field be rotated and reflected appropriately so that it corresponds to the simulation's Cartesian axes. The fields are extracted from the interpolated table values as follows

$$\begin{aligned} \mathbf{E}_{S,i} &= \frac{q_i}{e} R_z(\theta_i) \mathbf{E}_{2d}(\rho_i, \zeta_i) \\ \mathbf{E}_{X,i} &= \mathbf{E}_{3d}(\rho_i, \zeta_i, \theta_i) \\ \mathbf{E}_{I,ij} &= \frac{q_j}{e} \mathcal{R}_y(\theta_i, \theta_j) R_z(\theta_i) \mathbf{E}_{5d}(\rho_i, \zeta_i, \rho_j, \zeta_j, |\theta_i - \theta_j|) \end{aligned} \tag{6.7}$$

where $R_z(\theta_i)$ denotes the rotation matrix around the $z$-axis by an angle $\theta_i$

and $\mathcal{R}_y(\theta_i, \theta_j)$ is a reflection operator on the $x$-$z$ plane defined by

$$\mathcal{R}_y(\theta_i, \theta_j) = \begin{cases} D(1,1,1), & \text{if } \pi > \theta_j - \theta_i > 0, \\ D(1,-1,1), & \text{if } 0 > \theta_j - \theta_i > -\pi. \end{cases} \tag{6.8}$$

Here $D$ denotes a diagonal matrix with entries as indicated in the arguments.

Once the field and potential are known, the force and potential energy on ion $i$ can be calculated from

$$\mathbf{F}_i = q_i \mathbf{E}_i, \tag{6.9}$$

$$U_i = q_i (V_i - \frac{1}{2} V_{S,i}). \tag{6.10}$$

Note that only half the self potential is used when calculating the potential energy, as explained earlier.

## 6.4 Testing

To test the accuracy of the lookup method, we compare the interpolation results for potential energy and force with those obtained from the analytical solution of Poisson's equation for a toroidal channel in a variety of situations. The channel boundary is generated by rotating a circle in the $x$-$z$ plane around the $z$-axis. The radius of the circle is 40 Å and its center is located at $x = 44$ Å, $z = 0$. Refer to chapter 4 for details of the analytical solution. The results of electric potential and each Cartesian component of the field for the self, external and image parts are stored in tables with dimensions $(37 \times 97)$, $(10 \times 171 \times 40)$ and $(7 \times 119 \times 7 \times 119 \times 14)$, respectively. These dimensions are found after an optimization of the lookup program for the toroidal channel. The catenary channel described in Fig. 3.1 has a similar shape, and lookup tables with the same dimensions are used in the BD simulations in the next chapter.

Among the three potential (or field) parts, the self potential displays larger errors compared to the image and external potentials. Therefore, in the following tests, we focus on the potential energy and the force on a single ion in a toroidal channel which has no other fixed charges or external fields. In Fig. 6.1, we show the potential energy and the $z$-component of the force for a single ion moving parallel to the central axis but offset from it by 3 Å. Since the $z$-component of the force provides the driving force in the BD simulations, only that one is shown in this figure. The solid lines are calculated from the analytical method, and the circles by interpolating from the pre-calculated values stored in the lookup tables. The spacing between points in the lookup table is 1.77 Å in the $z$-direction, and the circles are at the midpoints of these intervals, where the maximum interpolation error is expected to occur. The radius of the channel varies with $z$, and hence the spacing between points in the $r$-direction changes. Therefore, the circles are

not necessarily located at the midpoints of the interpolation intervals in the radial direction.

The relative error for the potential and force are not shown in a separate graph because they are less than 1% for all the points in Fig. 6.1. Almost identical results are obtained for other ion trajectories parallel to the central axis but with different radial offsets. In Fig. 6.2, we show a similar plot of the potential energy and the radial component of the force in the $z = 0$ plane as the ion is moved radially from the central axis towards the boundary. Note that the closest approach is limited by the size of the ion. Here the circles correspond to the midpoints of the interpolation intervals in both the $z$ and the radial directions. The relative error is again less than 1% for all the points in Fig. 6.2. In Fig. 6.3, we show another comparison for the potential energy and the radial component of the force on a radial trajectory in the $z = 30$ Å plane. Again the circles are chosen at the midpoints of the interpolation intervals. The relative error remains less than 1% for the potential but rises to a few percent for the force for points near the boundary in Fig. 6.3. The agreement between the analytic and lookup methods evident in Figs. 6.1, 6.2, and 6.3 indicates that the interpolation error is negligible for the potential energy and the $z$-component of the force in the most important parts of the channel.

Tests carried out on a catenary channel yield a similar agreement between the lookup method and the numerical solution results. The relative error is slightly larger when an ion approaches the vestibular wall in the catenary channel, but this is not of great concern in simulations since ions tend to stay away from the water-protein boundary.

The system of generalized coordinates we use has a weakness at the entrance to the pore, where the boundary runs horizontally, perpendicular to the $z$-axis. The radius suddenly jumps from that of the reservoir to that of the pore entrance. This results in spurious interpolation between points near the channel's top surface and points in the pore entrance. Errors in the potential near the channel's top surface are unlikely to affect the results of simulations. Errors in the potential in the pore entrance are of greater concern. The magnitude of the force is rather small in this region, however, and we have checked in control runs that it has no effect on the simulations. An improved system of generalized coordinates that avoids this problem may be desirable in other applications of this method.

## 6.5 Performance

The use of lookup tables is practical despite the large number of points at which the field needs to be calculated, because the time used by the algorithms depends much more on the number of solutions needed rather than the number of points per solution. Both the iterative and analytical

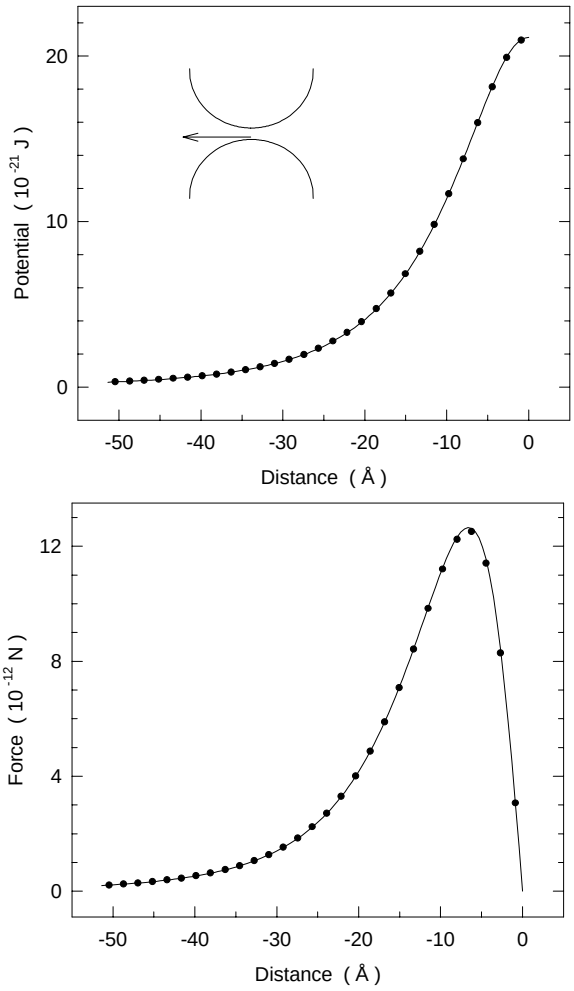


Figure 6.1: Comparison of the potential energy and the $z$-component of force, obtained from the lookup tables by interpolation (circles), with the analytical solutions (lines) for a toroidal channel. An ion is moved along the trajectory that is parallel to the central axis but is offset from it by 3 Å, as indicated by the arrow in the inset. The position of each circle in the $z$-direction is located at the midpoint between two adjacent points stored in the lookup table.

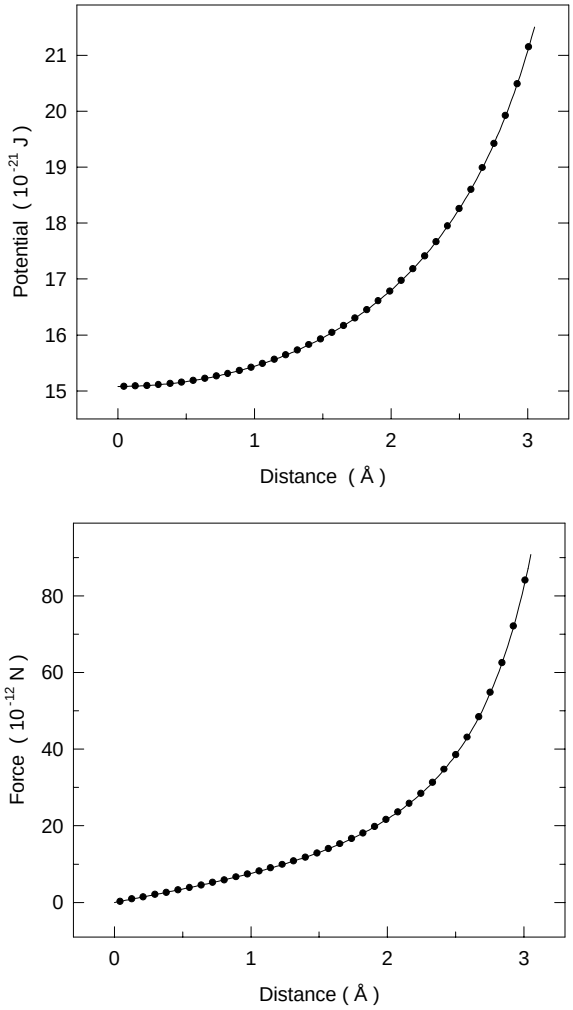


Figure 6.2: Same as Fig. 6.1 but for a radial trajectory in the $z = 0$ plane. The lookup results (circles) are calculated at the midpoints of the interpolation intervals in both the $z$ and the radial directions.

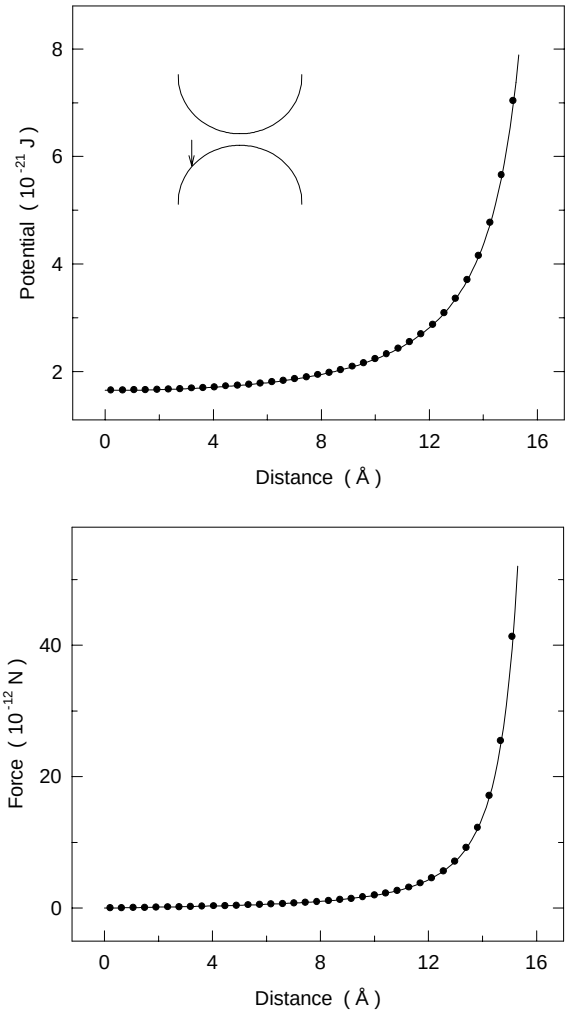


Figure 6.3: Same as Fig. 6.2 but for a radial trajectory in the $z = 30$ Å plane (see inset).

algorithms can easily generate the field at multiple points arising from many charges at given positions (which we call one solution). On the VPP a solution for 50 ions and 16 fixed charges takes 0.4 s (of CPU time) by the analytical algorithm, 2 s by the iterative algorithm, but only 0.006 s by the lookup table method. A BD simulation of 2 million steps would thus take 220 hours by the analytical algorithm, 46 days by the iterative method, and 3 hours by the lookup table method. The filling of the tables takes only an hour using the analytical solution and 10 hours using the iterative solution. To give an example, generating a 5d lookup table using the iterative method (which is the most time consuming) requires only 833 solutions, each for a single ion and at 12000 points. Each solution takes 21 s and the total time required is about 5 hours. Another advantage of the method is that once the tables are constructed for a given geometry, they can be used in many simulations studying different aspects of channel conductance.